

www.solar-rrl.com

Understanding Silicon Heterojunction Solar Cells with nc-SiC/SiO₂ as an Alternate Transparent Passivating Front Contact and Computational Design Optimization

Habtamu Tsegaye Gebrewold,* Karsten Bittkau, Kaifu Qiu, Uwe Rau, and Kaining Ding

The potential performance of silicon heterojunction solar cells applying transparent passivating contact (TPC) at the front side, based on a nc-SiC:H/SiO2 layer stack, is modeled and investigated. Herein, a complete multiscale electro-optical device model of TPC solar cells is developed. The model is then used to understand and analyze such cells and search for potential conversion efficiency improvement paths. The influences of contact layer thicknesses and other properties on device performance are studied. An algorithm-based optimization of cell electro-optical performance is performed. It is implemented by coupling a genetic algorithm with a finite element method-based TPC solar cell device model. Optimum front contact layer thicknesses are calculated. For optically optimized TPC contact layer thicknesses, an optical improvement of around 0.5 mA cm⁻² is found. Moreover, for complete electro-optical optimization of TPC layers, about 0.27% absolute value increment in power conversion efficiency is calculated. At the rear side, proper designing of optimizing carrier transport using active dopant concentration of p-type a-Si:H layer and indium tin oxide layer has shown a potential to reach power conversion efficiency beyond 25%.

1. Introduction

Silicon solar cells are getting closer to their practical limit.^[1–8] The main reasons are improvements in wafer quality, improved

H. T. Gebrewold, K. Bittkau, U. Rau, K. Ding IEK-5 Photovoltaics Forschungszentrum Jülich GmbH 52425 Jülich, Germany E-mail: h.gebrewold@fz-juelich.de

H. T. Gebrewold, U. Rau Faculty of Electrical Engineering and Information Technology RWTH Aachen University 52074 Aachen, Germany

K. Qiu Zhejiang Aiko Solar Energy Technology Co., Ltd Yiwu 322009, P. R. China

The ORCID identification number(s) for the author(s) of this article can be found under https://doi.org/10.1002/solr.202201051.

© 2023 The Authors. Solar RRL published by Wiley-VCH GmbH. This is an open access article under the terms of the Creative Commons Attribution-NonCommercial-NoDerivs License, which permits use and distribution in any medium, provided the original work is properly cited, the use is noncommercial and no modifications or adaptations are made.

DOI: 10.1002/solr.202201051

light management, electrical contact design, and good surface passivation. Further progress of such cells demands a very good understanding of different aspects of the device characteristics, including multiscale optical and electrical properties. Hence, an accurate electro-optical device modeling of such cells plays a vital role in understanding and designing an improved cell performance while appreciating the complexity of the impacts of changing a specific property in a device. One of the important developments in silicon solar cells in recent years is the improvement of passivation of the silicon surface. In this regard, record silicon solar cells in recent years are evident. Examples of such cells include tunnel oxide passivated contact (TOPCOn),[9] poly-Si on oxide (POLO),[10] and silicon heterojunction (SHJ)[1,6,7,11] technologies. They all use poly-Si or hydrogenated a-Si:H layers as a passivation layer

deposited on the silicon wafer surface. Despite their good passivation benefit, these layers absorb photons, creating short-lived electron-hole pairs. All or a significant fraction of these generated electron-hole pairs will be lost through recombination without a significant contribution to charge carrier collection at the terminal of the device. For example, in SHJ cells, only around 30% of charge carriers generated in the intrinsic a-Si:H layer are collected to contribute to the terminal current. [12,13] As a result, parasitic absorption is still an issue, especially on the front side of such well passivated cells. Alternative options to reduce such parasitic optical absorption include: 1) interdigitated back contact (IBC)^[1,10] and 2) replacing the passivating contact layers with more transparent materials with good passivation and conductivity.[14] The former option involves too many processes and fabrication steps; as a result, it is a costly and not viable option for large-scale production. [15–17] The latter option involves finding a wide bandgap material that is transparent to the relevant light spectrum. However, it must also provide good passivation and have an acceptable conductivity level for carrier transport.

As a wide bandgap material, silicon carbide is an interesting transparent material. [14,18-20] Köhler et al. have shown that a proper deposition of multilayer nanocrystalline silicon carbide together with tunnel oxide (SiO₂) layer can be an option providing not only transparency but also passivation and an acceptable

www.advancedsciencenews.com

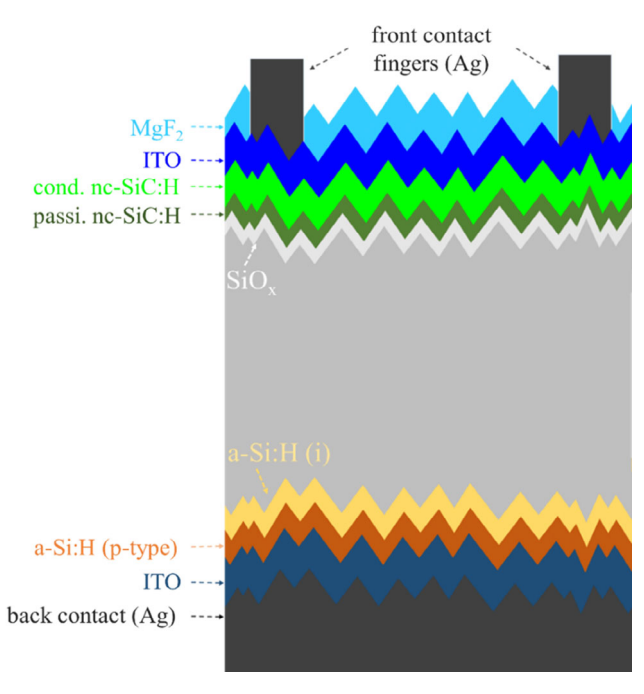


Figure 1. Cross-sectional view of crystalline silicon solar cell with TPC layers stack at the front side and a-Si:H-based SHJ at the rear side.

level of conductivity. [14] Such a stack of layers providing transparency, passivation, and conductivity is called transparent passivating contact (TPC) and will be used as such for the remainder of this work. For a SHI solar cell with TPC front contact instead of amorphous silicon layers, a short-circuit current density up to $40.9\,\mathrm{mA\,cm}^{-2}$ and power conversion efficiency up to a value of 23.99% have been achieved so far. These values of short-circuit current density and power conversion efficiency are certified, by ISFH-CalTEC, for the record TPC contact solar cell developed in our institute. [14] The cross-sectional view sketch of a TPC cell is shown in Figure 1. Exploiting the potential of such TPC cells requires further understanding and investigation. In this work, we try to develop an optoelectric model of such a cell, accounting for the complex aspects of the device physics as complete as possible. The model was validated with the experimental data. The validated simulation model is then used to understand, investigate, and assess pathways for further improvement potential of TPC solar cells.

2. Numerical Model

2.1. Optical Model

Optical simulation of a TPC cell is performed using Sentaurus TCAD.^[21] It is implemented as a multiscale optical simulation, i.e., a raytracing model coupled with a transfer matrix method (TMM). TMM is needed for the wave optics model of thin contact layers. The optical properties used are measured by ellipsometry. The refractive indices of the materials used are given in Figure S1, Supporting Information. To account for parasitic absorption due to plasmonic effects at the rear indium tin oxide

www.solar-rrl.com

(ITO)/Ag interface, we inserted an interlayer of an effective medium of ITO and Ag mixture in between. Looyenga effective medium approximation (EMA) is used to calculate the effective dielectric constant of the interlayer. [22] For a simplistic assumption of equal volume mixture, the complex effective dielectric constant ($\varepsilon_{\rm eff}$) is given as

$$\varepsilon_{\text{eff}} = \frac{1}{8} (\sqrt[3]{\varepsilon_{\text{ITO}}} + \sqrt[3]{\varepsilon_{\text{Ag}}})^3 \tag{1}$$

where $\varepsilon_{\rm ITO}$ and $\varepsilon_{\rm Ag}$ are the complex dielectric constant of ITO and silver, respectively. The refractive index $(n_{\rm eff})$ and extinction coefficient $(k_{\rm eff})$, calculated using the relation $(n_{\rm eff}+j*k_{\rm eff})^2=\varepsilon_{\rm eff}$, are also given in Figure S1, Supporting Information.

The optical simulation is limited to a smaller sample size ($10\,\mu\mathrm{m}\times10\,\mu\mathrm{m}$) 3D simulation for practical reasons, time, and resources. Moreover, the electrical simulation is done in a 2D half-pitch sample size accounting for the electrical effects of the metal finger contact width and pitch on the device performance. However, the 3D optical generation profile cannot be used directly for electrical simulation in a 2D half-pitch sample size. Hence, we used an approximate 2D generation profile based on the 3D optical simulation. For this, the total generated electron–hole pair concentration rate or the photogenerated carrier flux ($N_{\mathrm{Total}}\,[\mathrm{s}^{-1}]$) in the c-Si layer is calculated from the 3D optical simulation. Then, a 1D approximate optical generation profile ($G(\lambda,\,\zeta)\,[\mathrm{cm}^{-3}\mathrm{s}^{-1}]$), see Equation (2), is calculated based on the Lambert–Beer law of propagation in a homogeneous medium.

$$G(\lambda, \zeta) = \frac{1}{A_{\text{surf}}} \frac{\alpha(\lambda) N_{\text{Total}}(\lambda, d_{\text{cSi}}) e^{-\alpha(\lambda)\zeta}}{(1 - e^{-\alpha(\lambda)d_{\text{cSi}}})}$$
(2)

where $A_{\rm surf}$ is surface area, ζ is the distance from the front surface, $\alpha(\lambda)$ is the absorption coefficient, $d_{\rm cSi}$ is the thickness of the c-Si layer, $N_{\rm Total}$ [s⁻¹] is the total photogenerated carrier flux in the c-Si layer, and λ is the wavelength of light.

Absorbed and photogenerated carrier flux are equal, considering a unity quantum yield, and they are used interchangeably here. Fell et al. calculate a generation profile by considering the first pass of rays to the rear surface, and then distribute the remaining photogenerated carrier flux evenly throughout the cell. [23,24] The remaining photogenerated carrier flux corresponds to the rays beyond the first pass to the rear surface. We, however, calculated a generation profile using the total absorbed photon concentration rate or total photogenerated carrier flux $(N_{\text{Total}}[s^{-1}])$ in such a way that it would get absorbed in a single pass from the front surface to the rear surface abiding by the Lambert-Beer law of exponential intensity decay. For wavelengths shorter than the corresponding wavelength at the c-Si bandgap, a single pass to the rear surface is a good approximation. Photons get absorbed before hitting the rear surface due to a very high absorption coefficient $\alpha(\lambda)$ [cm⁻¹]. For longer wavelengths, i.e., near the c-Si bandgap, light rays are trapped and propagate back and forth multiple times before escaping. Due to these multiple paths, the generated electron-hole pair density rate is relatively uniform compared to the density for the part of the light spectrum at shorter wavelengths (see Figure S2, Supporting Information). Therefore, the shape of a longitudinal

Solar

www.advancedsciencenews.com www.solar-rrl.com

optical generation profile is determined mainly by the part of the light spectrum for wavelengths well below the bandgap. An x-zplanar cross section of the 3D optical generation profile is provided for different wavelengths in Figure S2, Supporting Information. We can see that laterally the generation profile for the total relevant spectrum (300-1200 nm) of AM1.5g is relatively uniform. Hence, an average laterally uniform optical generation profile is a good enough approximation. A comparison of a generation profile calculated as exponential decay of the total photogenerated carrier flux, using Equation (2), against an average of 1D profiles cut in x and y direction in 0.5 μ m steps from the 3D optical generation profile (see Figure S3, Supporting Information) shows an agreement except for the bump around $\zeta = 20 \,\mu\text{m}$. It could be a light focusing effect of the random-sized pyramid textures. Furthermore, one should note that the 1D profile average from the 3D optical generation profile involves shifting meshing points on the textured surface to the same plane at z = 0. It may introduce numerical artifacts.

2.2. Electrical Model

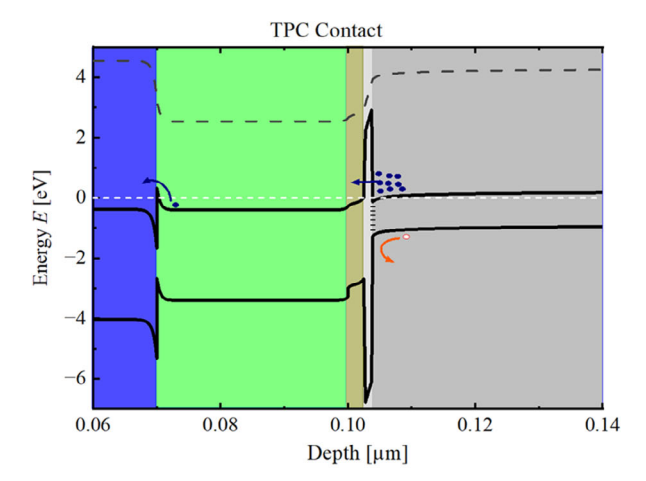
Using the output of the optical simulations as an input, as discussed above, finite element method-based electrical simulation is implemented using Sentaurus TCAD. Carrier transport at the TPC contact side is limited by direct tunneling through the thin oxide layer (see **Figure 2**) and lateral transport in the ITO layer. The direct tunneling is calculated using Wentzel–Kramers–Brillouin (WKB) approximation through the barrier oxide layer. The carrier transport at the SHJ contact (see Figure 2) is mainly limited by the band-to-band tunneling at the p-doped a-Si:H/ITO interface and trap-assisted tunneling in the amorphous layers. Carrier tunneling is modeled using the nonlocal tunneling model as implemented in Sentaurus TCAD with effective tunneling masses in **Table 1**. [21]

Consistently used parameters for the model in this work are given in Table 1. Material and interface parameters will be mentioned while discussing it; otherwise, the parameters mentioned in Table 1 and S1, Supporting Information, are considered.

2.3. Electro-Optical Device Optimization via Genetic Algorithm

Thickness optimization by varying layer thicknesses is time-consuming and resource-demanding; in many cases, as the number of parameters to consider grows, it becomes rather unpractical. In such a case, optimization using an appropriate algorithm is important. Here, we used a genetic algorithm (GA). For this, an open-source python library called PyGAD, developed by Ahmed F. Gad, was adapted to synchronize with the device simulation model. [25] In GA, individual parameters are considered as genes. Collections of these genes are chromosomes. A set of chromosomes is categorized as a population corresponding to a single generation. Each chromosome has an associated fitness value. The initial population can be predefined or randomly generated within given bounding limits of values set for each gene. These limits need to be practically meaningful under the context of the work.

In this work, a gene represents a thickness of a layer, a chromosome is a set of thicknesses of each layer under consideration for optimization, which are the front contact thin layers of TPC cell (MgF2, ITO, conductive nc-SiC:H, and passivating nc-SiC:H), and a population represents a set of chromosomes with a different combination of layer thicknesses in a single generation or iteration. At the start (first generation), one of the chromosomes consists of the thicknesses corresponding to our measured cell, and the other chromosomes consist of random thicknesses within the bounding limits set. The bounding min and max limits used in this work are 0 and 200 nm for MgF₂, 0 and 150 nm for ITO, 1 and 100 nm conductive nc-SiC:H, and 0 and 20 nm for passivating nc-SiC:H. Fitness values are optical photocurrent density, I_{ph} [mA cm⁻²], for optical optimization and power conversion efficiency, η [%], for electro-optical optimization, both calculated via the device model. After each generation, chromosomes are sorted according to their fitness values. The fittest chromosomes will be selected for mating as a parent, and variation operations are applied to create offspring and pass them to the next generation. In this work, the top 4 fit parents are selected from the population size of 8. The population size is chosen to fit the number of nodes



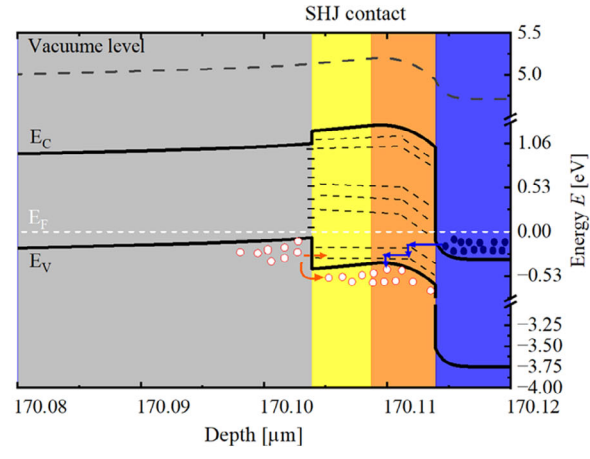


Figure 2. Band diagram of a TPC solar cell: TPC front contact layers on the left and SHJ bottom contact on the right side. The colors correspond to each layer similar to the cross-sectional view of a TPC solar cell as shown in Figure 1.

www.advancedsciencenews.com www.solar-rrl.com

Table 1. Summary of consistent input parameters used for simulations of TPC solar cells.

Optical input					
Solar spectrum	spectrum AM1.5g				
Generation profile		Section 2.1, Equation (2)			
c-Si					
Free carrier statistics		Fermi	–Dirac		
Temperature		30	0 K		
Auger and radiative recombination		Richter et al., ^[26]	Nguyen et al. ^[29]		
Intrinsic carrier density	Altermatt et al. $^{[30]}$ (9.65 × 10 9 cm $^{-3}$ at $T = 300$ K)				
Wafer resistivity	$1.0 \Omega \text{cm}, \text{ n-type}/N_D = 4.945 \times 10^{15} \text{cm}^{-3}$				
Mobility	Klaassen ^[31]				
Bulk SRH lifetime	20 ms				
Thickness		170	μm		
TPC side contact ^{a)}	SiO ₂	Passiv. nc-SiC:H	Cond. nc-SiC:H	ITO	
Thickness [nm]	1.4	2.5	30	70	
Band gap [eV]	9.0	2.7	3.0	3.7	
Electron affinity [eV]	0.9	2.93	2.93	4.9	
Dielectric constant	3.9	9.66	9.66	4.7	
Electron mobility [cm ² V ⁻¹ s ⁻¹]	_	1.56×10^{-7b}	4.46×10^{-3b}	27.6	
Barrier tunneling mass (electron/hole)* m_0^{c}	(0.73/0.4)	(0.73/0.4)	(0.73/0.4)	_	
Active dopant concentration [cm ⁻³]	_	2.0×10^{20}	7.0×10^{20}	1.68×10^{20}	
Effective DOS $(N_{\rm C}/N_{\rm V})$ [cm ⁻³]	-	$(1.6/1.2) \times 10^{19d}$	$(1.6/1.2) \times 10^{19d}$	$(0.4/1.7) \times 10^{196}$	
SHJ side contact	a-Si:H(i)	a-Si:H(p)	ІТО		
Thickness [nm]	5	5	100		
	,		,		

SHJ side contact	a-Si:H(i)	a-Si:H(p)	ІТО
Thickness [nm]	5	5	100
Band gap [eV]	1.7 ^{e)}	1.7 ^{e)}	3.7 ^{e)}
Electron affinity [eV]	3.9 ^{e)}	3.9 ^{e)}	4.9 ^{e)}
Dielectric constant	11.7 ^{e)}	11.7 ^{e)}	4.7
Electron mobility [cm² V ⁻¹ s ⁻¹]	20/4 ^{e)}	25/5 ^{e,g,h)}	22.0
Barrier tunneling mass (electron/hole)* $m_0^{ m c)}$	0.1/0.1 ^{f)}	0.1/0.1 ^{f)}	0.1/0.1 ^{f)}
Active dopant concentration [cm^{-3}]	_	9.5×10^{19}	1.4×10^{20}
Effective DOS ($N_{\rm C}/N_{\rm V}$) [cm ⁻³]	$(2.0/2.0) \times 10^{20e)}$	$(2.0/2.0) \times 10^{20e}$	$(0.4/1.7) \times 10^{19e}$

Materials and interfaces traps

SiO ₂ /c-Si interface	See Table S1, Supporting Information
c-Si/a-Si:H interface	See Table S1, Supporting Information
a-Si:H (i and p) materials	See Table S1, Supporting Information

a)TPC contact refers to the front thin film layers before MgF₂ antireflection coating layer deposition; b)Adapted from measured conductivities^[32]; c)m₀ is electron rest mass; d)ref. [33]; e)ref. [34]; f)ref. [35]; g)ref. [36]; h)ref. [24].

we have to compute simulations in parallel. The variation operations are crossover and mutation. A single-point crossover is used in this work. Two chromosomes give parts of their gene sequence (i.e., parameter list) to create a new chromosome. This allows the passing of desired characteristics from selected parents into offspring. Mutation of 40% of genes of a chromosome is allowed. The resulting new set of chromosomes represents the next generation.

3. Current Losses of TPC Cell

The optical simulation result of a TPC cell is shown in **Figure 3**a. Here, 120 nm of MgF_2 is deposited as an antireflection coating on top of a TPC cell depicted in the cross-sectional sketch in Figure 1. A shading fraction of 3.5% is assumed to account for the shading loss due to the fingers of the front metallization. It is the ratio of front contact fingers areal coverage with respect

and-conditions) on Wiley Online Library for rules of use; OA articles are governed by the applicable Creative Commons

www.solar-rrl.com

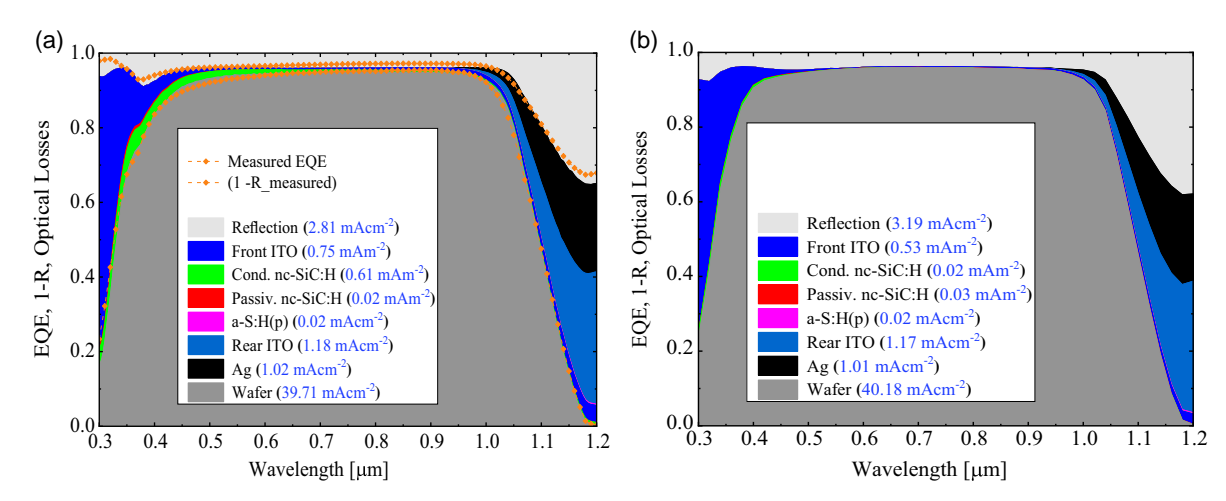


Figure 3. a) EQE and reflectance measurement versus simulation and current losses. The front layer thicknesses are 120 nm MgF₂, 70 nm ITO, 30 nm conductive nc-SiC:H, and 2.5 nm passivating nc-SiC:H. b) Thickness optimization using a GA gave an optimized EQE for the front thicknesses of 110.2 nm MgF₂, 44.2 nm ITO, 1.5 nm conductive nc-SiC:H, and 3.0 nm passivating nc-SiC:H. The photocurrent increased by 0.47 mA cm⁻², which is a 1.2%rel. increment. We considered, in both cases, a 3.5% shading loss to account for the shading effect of front metallization.

to the pitch. On the rear side, an interlayer between ITO and Ag is assumed, as described in Section 2.1. Our simulation fits the experiment well. In Figure 3, photocurrent corresponding to external quantum efficiency (EQE) and current losses are calculated for TPC solar cells. The reflection loss (2.81 $\rm mA\,cm^{-2})$ is the highest current loss, followed by a parasitic loss at the rear side ITO and Ag layers (total 2.2 $\rm mA\,cm^{-2})$). The current loss at front ITO (0.75 $\rm mA\,cm^{-2})$ and nanocrystalline silicon carbide layers (0.63 $\rm mA\,cm^{-2})$ are also significant.

3.1. Optical Optimization of Front Contact Layer Thicknesses

To reduce parasitic losses at the front layers and increase optical generation in the silicon, optical optimization using a GA is implemented for front layer thicknesses. Thicknesses of the thin front contact layers of TPC cell, which are MgF₂, ITO, conductive nc-SiC:H, and passivating nc-SiC:H, are parameters to be varied and used as genes in GA. Photogeneration current (J_{ph}) is used as a fitness function. Then, optical optimization of TPC cells based on the front contact layer thickness is conducted, and the result is given in Figure 4. Our simulation shows that a gain of at least 0.5 mA cm⁻² in short-circuit current density can be obtained through front contact layer thickness optimization. The corresponding thicknesses for the fittest or optimized cell are 110.2 nm MgF₂, 44.2 nm ITO, 1.5 nm conductive nc-SiC:H, and 3.0 nm passivating nc-SiC:H. Furthermore, the current losses for such optimized front contact thicknesses can be seen in Figure 3b. One can see that the gain is mainly due to the reduction of parasitic absorption in ITO and conductive nc-SiC:H layers due to smaller thicknesses.

In Figure 4, the optimal thicknesses are achieved in the 30th generation and stay similar for the next 75 generations. The Monte Carlo-based raytracing simulation is responsible for the small-scale scatter in Figure 4. In our optimization implementation, we do not keep the simulation for the fittest gene of

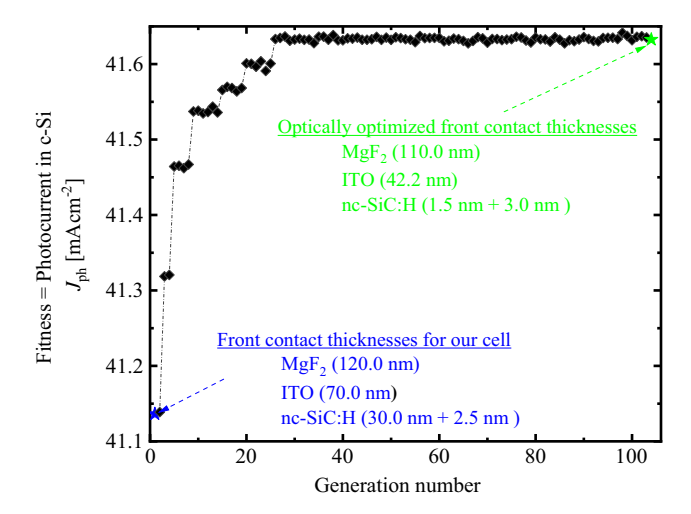


Figure 4. The fitness value of the fittest chromosome in the corresponding generation versus generation number of each offspring for optical optimization of TPC cell. For each set of thicknesses, photocurrent in c-Si is calculated using a 3D model of optical simulation based on raytracing combined with TMM method. The photocurrent is then used as a fitness value in the GA. Note that this plot does not include a shading loss of around 3.5%.

the previous generation. However, we do the optical simulation for each parameter set in every generation. It allows us to see the fluctuation due to Monte Carlo-based raytracing simulation when performed with less computational demand. Simulation with low computational demand is crucial when the number of simulations needed to arrive at the optimum value gets very high. It will be so when the number of parameters to consider increases. So far, we have tried to optimize the optical aspect of the device without considering its consequences on its electrical properties. Optimization accounting for both optical and electrical aspects is done in Section 4. It includes the study of front ITO and conductive nc-SiC:H layer thicknesses. However, we must

nditions) on Wiley Online Library for rules of use; OA articles are governed by the applicable Creative Commons

www.advancedsciencenews.com

www.solar-rrl.com

first validate our electro-optical device model described in the next section.

3.2. Validation of the Electrical Model

The optical simulation result, i.e., the optical generation profile that corresponds to the 3D optical simulation given in Figure 3a, is used as an input to the electrical simulation. The numerical model of a TPC cell is then validated with experimental measurements. The short-circuit current density was underestimated as compared to the measurement. It is due to different shading effects for EQE and current density-voltage measurements. Hence, we compensated for the short-circuit current density in the electrical model by scaling the whole current density versus voltage curve to fit the experimental short-circuit current density value. Our simulation and measurement data are in good agreement otherwise. The validation includes comparing current density versus voltage curve for a different number of suns, including 0.8, 1.0, and 1.2 Sun (see Figure 5). We also compared the I_{SC} - V_{OC} curve, giving a good agreement.

The corresponding cell performance parameters such as I_{SC} , $V_{\rm OC}$, FF, and efficiency η are compared in **Table 2**.

The recombination losses, in mA cm⁻², at short-circuit (SC) condition and maximum power point (MPP) are given in **Table 3.** The total recombination loss J_{rec} is the sum of Auger J_{aug}, radiative J_{rad}, Shockley–Read–Hall J_{srh}, and surface

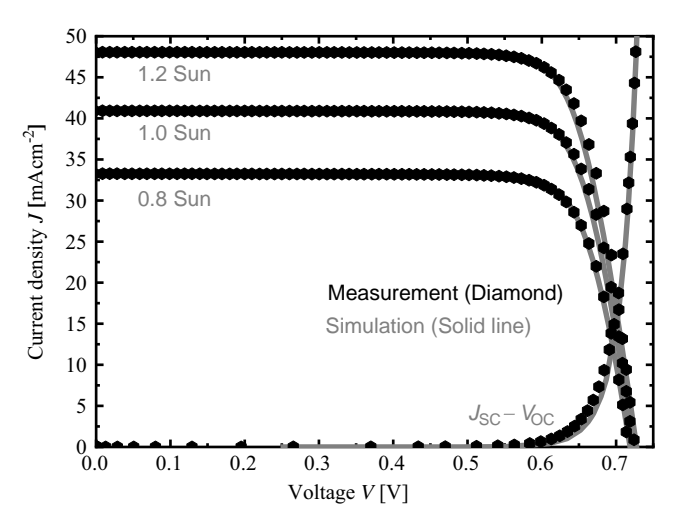


Figure 5. Experiment versus simulation of crystalline silicon solar cell with TPC layers stack at the front side and a-Si:H-based SHJ at the rear side (TPC-SHJ solar cell). TPC-SHJ solar cell's J(V) for a different number of suns and J_{SC}-V_{OC} curve. Note that this result includes the MgF₂ antireflection layer on top of the TPC-SHJ solar cell.

Table 2. In-house measured parameters for a TPC champion cell after the MgF₂ evaporation versus TCAD simulated cell data are shown.

Measurement/TCAD model	Efficiency η [%]	J _{SC} [mA cm ⁻²]	V _{OC} [mV]	FF [%]
Measurement	23.8	40.9	723	80.4
TCAD model	23.81	40.92	724	80.39

Table 3. Recombination losses at SC condition and MPP.

	$J_{ m rec}$	Jaug	J_{rad}	J_{srh}	J_{surf}
Unit	$\rm mAcm^{-2}$				
SC	0.07	0.03	0.01	0.03	0.00
MPP	1.71	0.36	0.10	0.22	1.02

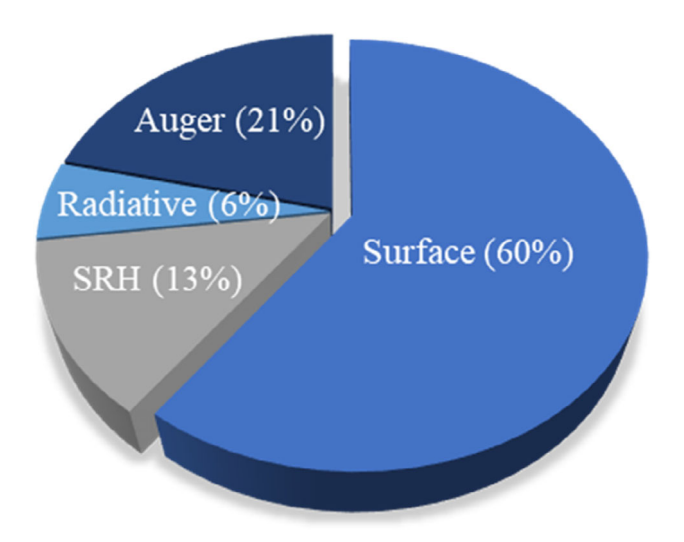


Figure 6. Individual recombination loss percentage at MPP.

recombination J_{surf}. At MPP, 60% of the recombination loss is due to surface recombination (see Figure 6). It signifies that the solar cell performance is limited by the passivation.

4. Device Performance Optimization

Here, we optimize the solar cell power conversion efficiency with a model for TPC cells that accounts for optical and electrical aspects. It includes thickness optimization of front contacts and doping concentration effect on carrier transport at the rear side.

4.1. Optimization of Front TPC Contact Layers Thickness

As discussed in the previous section, optical optimization of front contacts results in improved short-circuit current density. However, power conversion efficiency worsens due to a lower fill factor (FF) (see Table 4). The FF was lowered mainly due to higher sheet resistance for lower ITO thickness. Therefore, we need to use an electro-optical model to find optimum front contact thicknesses giving an optimal power conversion efficiency. For this, similar to the optical optimization, we coupled the GA with the TPC solar cell's numerical simulation. The GA takes power conversion efficiency as a fitness function. Our optimization starts from our measured device parameters as initial. The optimization reached an optimum power conversion efficiency value (24.09%) calculated within the 40th generation (see Figure S4, Supporting Information). Afterward, it stays similar except for small-scale scatter similar to the optical simulation.

www.advancedsciencenews.com www.solar-rrl.com

Table 4. TPC solar cell performances for optimized front contact thicknesses.

	Efficiency η [%]	$J_{\rm SC}~[{ m mAcm}^{-2}]$	V _{OC} [mV]	FF [%]
Measurement	23.8	40.9	723	80.4
TCAD model	23.81	40.92	724	80.39
Optical optimization ^{a)}	23.67	41.40	724	78.98
Electro-optical optimization ^{b)}	24.09	41.14	724	80.89

a) Optically optimized front contact thicknesses: 110.2 nm MgF₂, 44.2 nm ITO, 1.5 nm conductive nc-SiC:H, and 3.0 nm passivating nc-SiC:H; b) Electro-optically optimized front contact thicknesses: 98.7 nm MgF₂, 68.9 nm ITO, 13.3 nm conductive nc-SiC:H, and 2.05 nm passivating nc-SiC:H.

The optimization was mainly a tradeoff between transparency and sheet resistance concerning ITO and conductive nc-SiC:H layers. The change in sheet resistance is due to layer thickness. However, the material properties of the layers are assumed to be unchanged with thickness. The optimal thicknesses were 69 nm ITO and 13 nm conductive nc-SiC:H in addition to around 99 nm MgF $_2$ as ARC. In Table 4, TPC solar cell performance parameters are given for the optimized cell in addition to the initial measured and optically optimized cell performances.

Contour plots in **Figure 7** show the solar cell performance sensitivity on the thickness variation. ITO was varied up to 20% with respect to the optimal thickness. For conductive nc-SiC:H, up to 35% variation in thickness with respect to the optimal thickness is considered. The $J_{\rm SC}$ clearly shows a higher value for the smallest

ITO and nc-SiC:H thicknesses as one would expect. It gives -0.56% and +0.44% changes on the J_{SC} of electro-optical optimization for the smallest and largest thicknesses, respectively. FF changes up to -1.29% for small ITO thickness and 0.39% for large ITO thickness. The maximum change in power conversion efficiency is -0.95% with respect to the electro-optical optimum value.

4.2. Optimization of Rear SHJ Contacts

The series resistance contribution from the rear side c-Si/a-Si:H(i)/a-Si:H(p)/ITO/Ag contact is significant in SHJ solar cells. [26,27] The main reasons are the band-to-band tunneling transport at the a-Si:H(p)/ITO interface and trap-assisted tunneling in amorphous silicon, which depends on the alignment between the valence band of a-Si:H(p) and the conduction band of ITO. It means higher work function ITO or/and low activation energy of a-Si:H(p) are advantageous in this respect. The activation energy of the a-Si:H(p) layer also determines band bending and field-effect passivation needed at the c-Si/a-Si:H(i)/a-Si:H(p) contact for extracting minority carriers from c-Si. In this study, we considered unchanged refractive indices of the rear side contact layers for different active dopant concentrations, assuming an insignificant optical effect on the cell performance.

4.2.1. N_A of a-Si:H(p)

Figure 8 shows the impact of active dopant concentration of p-type a-Si:H layer on cell performances. Above $N_{\rm A}$ of $1\times10^{20}\,{\rm cm^{-3}}$, the cell performance saturated, indicating a proper alignment of the

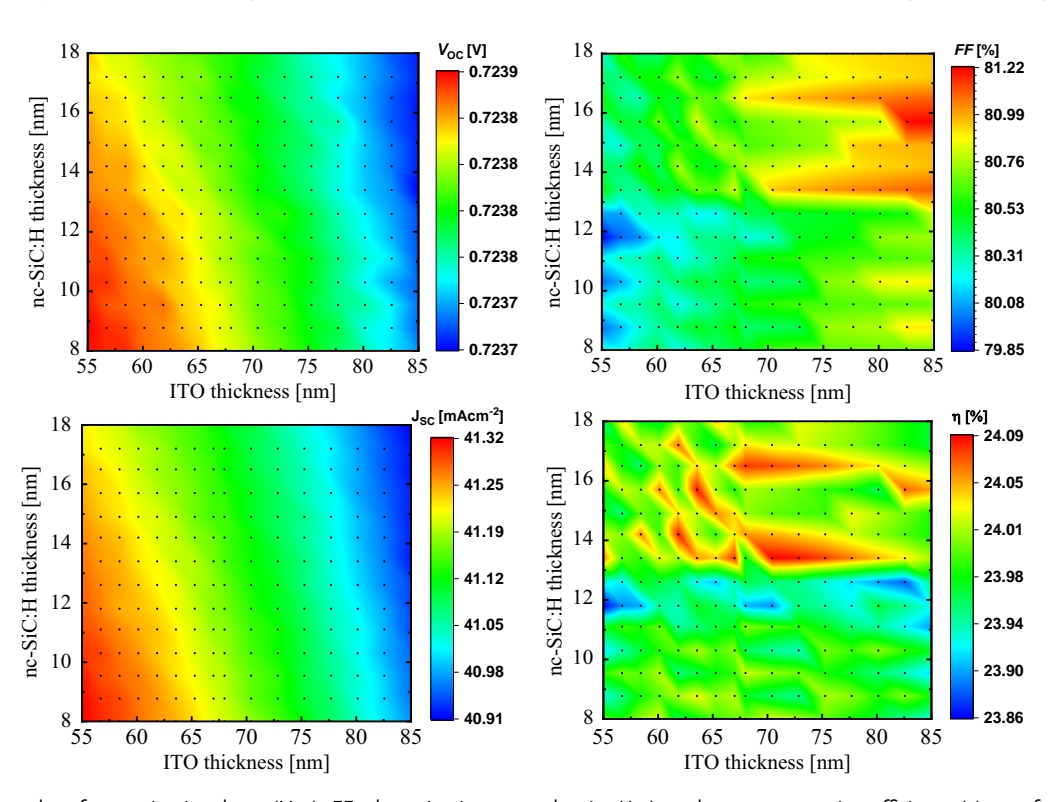


Figure 7. Contour plot of open-circuit voltage (V_{OC}), FF, short-circuit current density (J_{SC}), and power conversion efficiency (η) as a function of thicknesses of front ITO and nc-SiC:H layers.

rch Center, Wiley Online Library on [04/04/2023]. See the Terms and Conditions (https://onlinelibrary.wiley.

and-conditions) on Wiley Online Library for rules of use; OA articles are governed by the applicable Creative Commons

www.solar-rrl.com

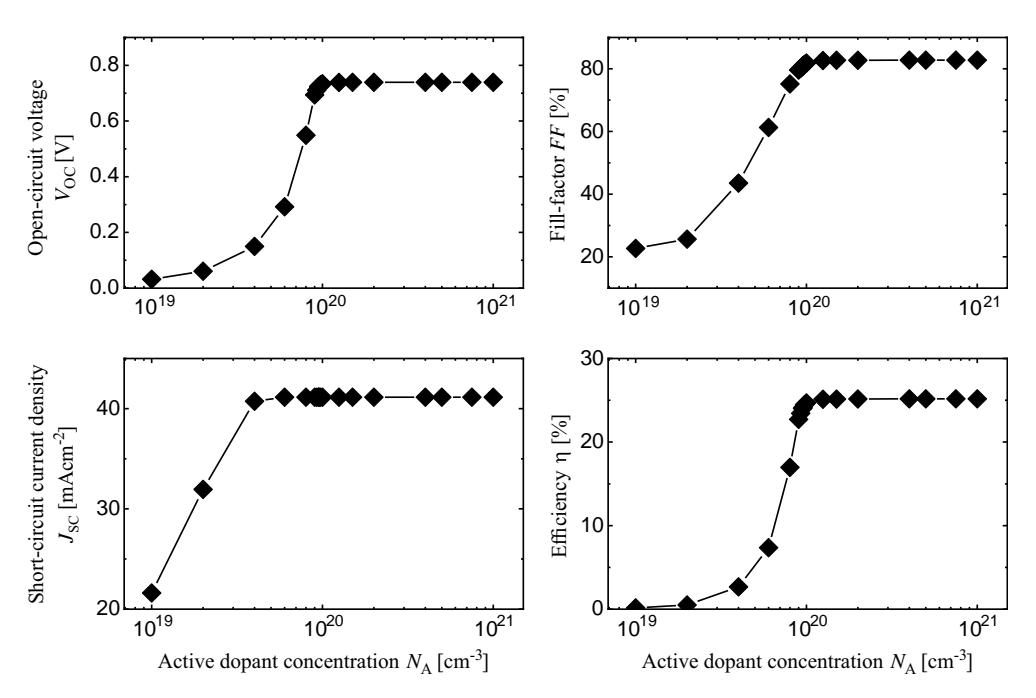


Figure 8. Open-circuit voltage (V_{OC}), FF, short-circuit current density (J_{SC}), and power conversion efficiency (η) as a function of active dopant concentration of a-Si:H(p) layer in TPC-SHJ solar cell for the optimized front contact layer thicknesses.

valence band of a-Si:H(p) with the conduction band of ITO above this value. For lower active dopant concentration, however, the defect and tail states in the amorphous layers are involved in minority carrier extraction of this contact. This is not an efficient process and will result in less extraction of minority carriers and high surface recombination.

Power conversion efficiency above 25%, $V_{\rm OC}$ around 739 mV, and FF around 82.7% can be achieved for higher active dopant concentration of a-Si:H(p). Proper optimization of carrier transport at the a-Si:H(p)/ITO can be modulated not only by using doping of a-Si:H(p) but also by the work function of ITO. Next, we present the effect of active dopant concentration of ITO on the TPC solar cell performance.

4.2.2. N_D of ITO and Thickness of a-Si:H(p)

TPC solar cell performances may not saturate at a high value of active dopant concentration in the ITO layer. It is unlike the case for the a-Si:H(p) layer. It signifies a negative effect on the space charge region for higher dopant concentration. [28] High free carrier concentration in ITO deteriorates the field-effect passivation and leads to enhanced recombination at the interface and amorphous layers. As a result, open-circuit voltage, FF, and power conversion efficiency deteriorate after a certain value of N_D (see the black curve in Figure 9). For low carrier concentration of ITO, similar to N_A of a-Si:H(p), the carrier transport at this contact will be facilitated by defect and tail states in the amorphous layers. It leads to inefficient minority carrier extraction and, therefore, inefficient solar cells. There is an interesting slight decrease in $V_{\rm OC}$ between $N_{\rm D}$ of $10^{19}\,{\rm cm}^{-3}$ and $4\times10^{19}\,{\rm cm}^{-3}$ before it jumps to high value of $V_{\rm OC}$ (see the black curve in Figure 9a). We suspect it is due to the transition of the role of midbandgap Gaussian defect states and bandgap tail states, and band bending near the a-Si:H(p)/ITO interface. It eventually jumps to dominant interband tunneling with less trap assistance.

From the discussion of the effect of N_D of ITO, one can deduce that there should be a tradeoff between carrier transport at a-Si:H(p)/ITO and the effect on space charge region or field effect passivation as suggested by S. Kirner et al. [28] However, we show it is possible to reduce the effect of a high free carrier concentration of ITO on the space charge region and field-effect passivation. This is so for a thick a-Si:H(p) layer. The red curve in Figure 9 is for a 20 nm a-Si:H(p) case. $V_{\rm OC}$ stayed similar for a whole range of N_D from 10^{17} cm⁻³ to 3×10^{20} cm⁻³ considered here. FF and, hence, power conversion efficiency saturated at high $N_{\rm D}$. For low $N_{\rm D}$, we see the same effect as discussed above for the case of 5 nm a-Si:H(p). However, the FF of the 20 nm case was lower than for the case of 5 nm a-Si:H(p) in the range of $N_{\rm D}$ below $2 \times 10^{19} \, {\rm cm}^{-3}$. It shows that for cases with no band alignment, the thickness of the a-Si:H(p) layer significantly affects the rear side contact's resistivity. It is because, in this case, trap-assisted tunneling is vital. Hence, the transport will degrade as the thickness of the amorphous layer increases, even for the doped p-type layer. However, this effect is not visible in the case of a proper valence band and conduction band alignment. Figure 10 shows the effect of a-Si:H(p) layer thickness for the electro-optical optimum front contact thicknesses. Low cell performance for thickness below 5 nm is due to a reduction in field-effect passivation. It improves up to 5 nm and saturates for larger thicknesses.

Using thick a-Si:H(p), the TPC cell performance of the electro-optical optimization in Table 4 can be improved to $V_{\rm OC}$ of 737 mV, FF of 82.2%, and η above 24.9%. As discussed above, for a high $N_{\rm A}$ of a-Si:H(p), an improved potential cell power conversion efficiency beyond 25%, $V_{\rm OC}$ around 739 mV, and FF around 82.7% can be achieved.

2367198x, 2023, 7, Downloaded

from https://onlinelibrary.wiley.com/doi/10.1002/solr.202201051 by Forsch

Wiley Online Library on [04/04/2023]. See the Term

rules of use; OA articles are governed by the applicable Creative Commons

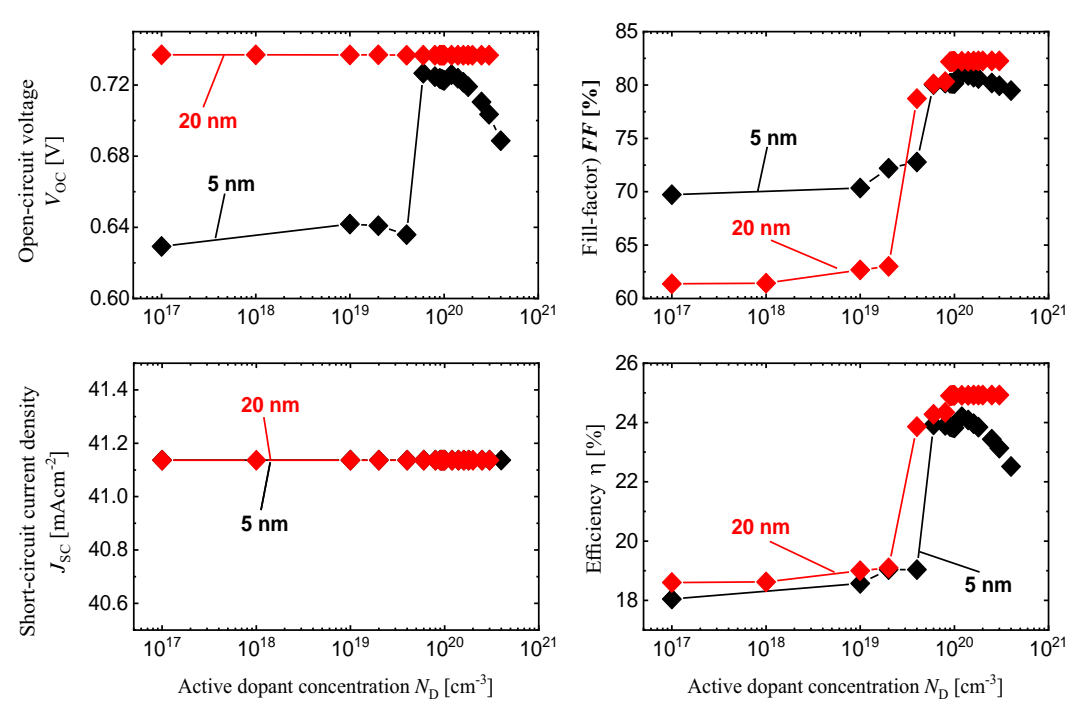


Figure 9. Open-circuit voltage (V_{OC}), FF, short-circuit current density (J_{SC}), and power conversion efficiency (η) as a function of active dopant concentration of rear side ITO layer in TPC-SHJ solar cell for the optimized front contact layer thicknesses.

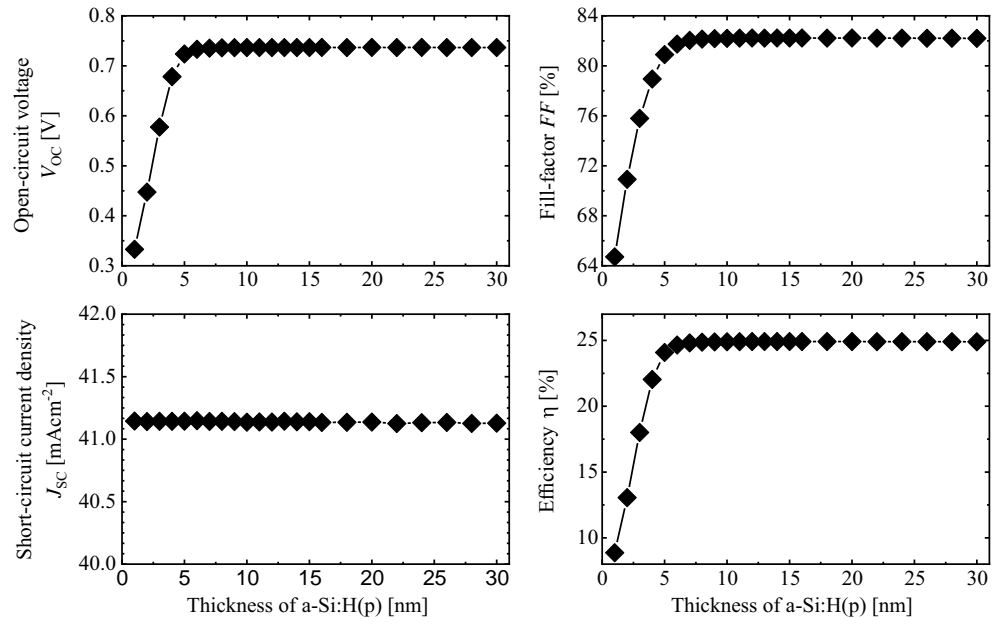


Figure 10. Open-circuit voltage (V_{OC}), FF, short-circuit current density (J_{SC}), and power conversion efficiency (η) as a function of thickness of a-Si:H(p) layer in TPC-SHJ solar cell for the optimized front contact layer thicknesses.

Further optimization of TPC solar cells needs investigation of different aspects beyond the scope of this work. These include optimizing the tunneling carrier transport at the front. For this, one needs to understand the nc-SiC:H layers' role in tunneling transport and field-effect passivation and optimize the oxide layer.

5. Conclusion

TPC solar cells are attractive because they combine the three most important solar cell front contact aspects. These are transparency to the visual and near-IR spectrum, passivation of the **ADVANCED** SCIENCE NEWS. Solar

www.advancedsciencenews.com www.solar-rrl.com

silicon surface, and carrier extraction and transport. A TPC front contact stack of ITO, nc-SiC:H bi-layer, and SiOx has already shown great potential on SHJ solar cells. In this work, we model such TPC solar cell accounting for optical and electrical aspects as complete as possible. The model is validated with experimental measurement. It is then used to predict the cell I(V) curves for different illumination levels to a good level of agreement. Using the model, we optimized front contact thicknesses, and carrier extraction and transport at the rear side. Genetic algorithmbased optimization of the TPC solar cell front contact thicknesses improves cell power conversion efficiency from 23.8% (measured) to about 24.1%. Optimizing hole extraction and transport at the rear side by changing active dopant concentration of p-type amorphous silicon layer showed an improved potential cell power conversion efficiency beyond 25%, V_{OC} around 739 mV, and FF around 82.7%. However, a high free carrier concentration in ITO can negatively affect field-effect passivation. This effect can be significantly reduced using a thick or high dopant concentration a-Si:H(p) layer.

Supporting Information

Supporting Information is available from the Wiley Online Library or from the author.

Acknowledgements

This work was supported by the Federal Ministry of Economic Affairs and Energy in the framework of the TUKAN project (grant no. 0324198D) and the (HEMF) Helmholtz Energy Materials Foundry infrastructure funded by the HGF (Helmholtz association). The authors would like to thank Dr. Pietro Altermatt for the fruitful discussion on Sentaurus TCAD at the start of the work.

Open Access funding enabled and organized by Projekt DEAL.

Conflict of Interest

The authors declare no conflict of interest.

Data Availability Statement

The data that support the findings of this study are available from the corresponding author upon reasonable request.

Keywords

genetic algorithms, numerical simulations, silicon carbides, silicon heterojunction solar cells, transparent passivating contacts

Received: November 23, 2022 Revised: January 9, 2023 Published online: January 29, 2023

- [1] K. Yoshikawa, H. Kawasaki, W. Yoshida, T. Irie, K. Konishi, K. Nakano, T. Uto, D. Adachi, M. Kanematsu, H. Uzu, K. Yamamoto, *Nat. Energy* 2017, 2, https://doi.org/10.1038/nenergy.2017.32.
- [2] M. A. Green, E. D. Dunlop, J. Hohl-Ebinger, M. Yoshita, N. Kopidakis, X. Hao, Prog. Photovoltaics Res. Appl. 2022, 30, 3.

- [3] L. C. Andreani, A. Bozzola, P. Kowalczewski, M. Liscidini, L. Redorici, Adv. Phys. X 2019, 4, 1548305.
- [4] R. M. Swanson, in Conf. Record of the Thirty-First IEEE Photovoltaic Specialists Conf.- 2005, IEEE 2005, p. 889.
- [5] A. Richter, M. Hermle, S. W. Glunz, IEEE J. Photovoltaics 2013, 3, 1184.
- [6] LONGi 2022, https://www.longi.com/en/news/indium-free-hjt/ (accessed: August 2022).
- [7] LONGi 2022, https://www.longi.com/en/news/new-hjt-world-record/ (accessed: August, 2022).
- [8] K. Yamamoto, K. Yoshikawa, H. Uzu, D. Adachi, Jpn. J. Appl. Phys. 2018, 57, 08RB20.
- [9] A. Richter, J. Benick, F. Feldmann, A. Fell, M. Hermle, S. W. Glunz, Sol. Energy Mater. Sol. Cells 2017, 173, 96.
- [10] F. Haase, C. Hollemann, S. Schäfer, A. Merkle, M. Rienäcker, J. Krügener, R. Brendel, R. Peibst, Sol. Energy Mater. Sol. Cells 2018, 186, 184.
- [11] SunDrive, https://www.pv-magazine.com/2021/09/10/australianstartup-sets-25-54-efficiency-record-for-silicon-cell/ (accessed: 2021).
- [12] Z. C. Holman, A. Descoeudres, L. Barraud, F. Z. Fernandez, J. P. Seif, S. de Wolf, C. Ballif, IEEE J. Photovoltaics 2012, 2, 7.
- [13] S. de Wolf, A. Descoeudres, Z. C. Holman, C. Ballif, Green 2012, 2, 7.
- [14] M. Köhler, M. Pomaska, P. Procel, R. Santbergen, A. Zamchiy, B. Macco, A. Lambertz, W. Duan, P. Cao, B. Klingebiel, S. Li, A. Eberst, M. Luysberg, K. Qiu, O. Isabella, F. Finger, T. Kirchartz, U. Rau, K. Ding, *Nat. Energy* **2021**, *6*, 529.
- [15] P. J. Verlinden, McEvoy's Handbook of Photovoltaics (Ed: S. A. Kalogirou), Academic Press, San Diego, USA 2017, p. 473.
- [16] G. López, P. R. Ortega, I. Martín, C. Voz, A. Orpella, R. Alcubilla, Energy Procedia 2016, 92, 652.
- [17] J. Haschke, Y.-Y. Chen, R. Gogolin, M. Mews, N. Mingirulli, L. Korte, B. Rech, Energy Procedia 2013, 38, 732.
- [18] F. Finger, O. Astakhov, T. Bronger, R. Carius, T. Chen, A. Dasgupta, A. Gordijn, L. Houben, Y. Huang, S. Klein, M. Luysberg, H. Wang, L. Xiao, *Thin Solid Films* 2009, 517, 3507.
- [19] M. Pomaska, M. Köhler, P. Procel Moya, A. Zamchiy, A. Singh, D. Y. Kim, O. Isabella, M. Zeman, S. Li, K. Qiu, A. Eberst, V. Smirnov, F. Finger, U. Rau, K. Ding, Prog. Photovoltaics Res. Appl. 2020, 28, 321.
- [20] M. B. Pomaska, *Doctoral thesis*, RWTH Aachen University, Aachen 2017.
- [21] Sentaurus™ Device User Guide, Synopsys, Inc., Mountain View, CA 2015.
- [22] H. Looyenga, Physica 1965, 31, 401.
- [23] A. Fell, K. R. McIntosh, in 2015 IEEE 42nd Photovoltaic Specialist Conf. (PVSC), IEEE, New Orleans, LA 2015, p. 1-5.
- [24] A. Fell, K. R. McIntosh, P. P. Altermatt, G. J. M. Janssen, R. Stangl, A. Ho-Baillie, H. Steinkemper, J. Greulich, M. Muller, B. Min, K. C. Fong, M. Hermle, I. G. Romijn, M. D. Abbott, *IEEE J. Photovoltaics* 2015, 5, 1250.
- [25] A. F. Gad, PyGAD: An Intuitive Genetic Algorithm Python Library 2021, arXiv:2106.06158.
- [26] A. Richter, F. Werner, A. Cuevas, J. Schmidt, S. W. Glunz, Energy Procedia 2012, 27, 88.
- [27] W. Duan, A. Lambertz, K. Bittkau, D. Qiu, K. Qiu, U. Rau, K. Ding, Prog Photovoltaics Res. Appl. 2021 https://onlinelibrary.wiley.com/doi/10.1002/pip.3493.
- [28] S. Kirner, M. Hartig, L. Mazzarella, L. Korte, T. Frijnts, H. Scherg-Kurmes, S. Ring, B. Stannowski, B. Rech, R. Schlatmann, *Energy Procedia* 2015, 77, 725.
- [29] H. T. Nguyen, S. C. Baker-Finch, D. Macdonald, Appl. Phys. Lett. 2014, 104, 112105.
- [30] Pietro P. Altermatt, Frank Geelhaar Andreas Schenk, Gernot Heiser, J. Appl. Phys. 2003, 93, 1598.

Solar

2367198x, 2023, 7, Downloaded from https://onlinelibrary.wiley.com/doi/10.1002/solr.202201051 by Forschungszentrum

and-conditions) on Wiley Online Library for rules of use; OA articles are governed by the applicable Creative Commons License

www.advancedsciencenews.com www.solar-rrl.com

- [31] D. Klaassen, Solid State Electron. 1992, 35, 953.
- [32] M. Köhler, *Doctoral thesis*, RWTH Aachen University, Aachen **2020**.
- [33] N. Lophitis, A. Arvanitopoulos, S. Perkins, M. Antoniou, in *Disruptive Wide Bandgap Semiconductors, Related Technologies, and Their Applications* (Ed: Y. K. Sharma), IntechOpen, London **2018**.
- [34] P. Procel, H. Xu, A. Saez, C. Ruiz-Tobon, L. Mazzarella, Y. Zhao, C. Han, G. Yang, M. Zeman, O. Isabella, Prog. Photovoltaics Res. Appl. 2020, 28, 935.
- [35] J. M. Shannon, K. J. B. M. Nieuwesteeg, Appl. Phys. Lett. 1993, 62, 1815.
- [36] M. Rahmouni, A. Datta, P. Chatterjee, J. Damon-Lacoste, C. Ballif, J. Appl. Phys. 2010, 107, 54521.